Gap-plasmon nanoantennas and bowtie resonators

Dmitri K. Gramotnev,[1,2] Anders Pors,[3,*] Morten Willatzen,[3] and Sergey I. Bozhevolnyi[2]
[1]*Nanophotonics Pty Ltd, GPO Box 786, Albany Creek, QLD 4035, Australia*
[2]*Institute of Technology and Innovation (ITI), University of Southern Denmark, Niels Bohrs Allé 1, DK-5230 Odense M, Denmark*
[3]*Mads Clausen Institute (MCI), University of Southern Denmark, Alsion 2, DK-6400 Sønderborg, Denmark*
(Received 8 September 2011; published 20 January 2012)

Plasmonic bowtie resonators involving gap surface plasmons (GSPs) in metal-insulator-metal (MIM) structures, in which only the top metal layer is structured, are investigated using numerical simulations. We demonstrate that the considered configuration features two efficiently excitable GSP resonances associated with distinct charge distributions with the domination of the dipole and quadrupole moments resulting in low- and high-Q resonances, respectively. The typical Q factors for the high-Q resonances are shown to achieve ~ 25 in the near-infrared, thus potentially exceeding the quasistatic limit. Detailed physical interpretations of the obtained results and consistent dependencies of the resonance characteristics on the geometrical structural parameters are presented. Excellent resonant characteristics, the simplicity of fabrication, and tuning of the resonance wavelength by adjusting the size of the bowtie arms, separation between them, and/or thickness of the insulator (SiO_2) layer in the MIM structure appear attractive for a wide variety of applications, ranging from surface sensing to photovoltaics.

DOI: 10.1103/PhysRevB.85.045434 PACS number(s): 73.20.Mf, 78.67.−n, 42.25.−p, 71.36.+c

I. INTRODUCTION

Plasmonic antennas and resonators [i.e., metal nanostructures exhibiting efficient (resonant) scattering of radiation and strongly enhanced local electromagnetic fields] have been a hot topic for intense theoretical and experimental investigation over the past few years.[1–19] The ever growing interest is impelled by the unique opportunities offered by these structures for the design of plasmonic nanosensors, nanomanipulation and near-field trapping techniques,[20,21] high-resolution probes for nanoimaging and information processing approaches,[18,19] improved photovoltaics,[22] nanoscale photodetectors with significantly enhanced signal-to-noise ratio,[23,24] catalysis applications,[24] efficient coupling of light energy to nanoscale structures, quantum dots and single molecules,[1–3] etc. Plasmonic nanoantennas are also expected to facilitate observation and applications of highly localized and enhanced nonlinear effects and near-field spectroscopy, including spectroscopic analysis, imaging and identification of nanoscale amounts of substances and single molecules,[1–3,24,25] and nanorefractometry.[26] Such a diversity of applications of plasmonic antennas and resonators implies that antennas with a wide range of optical properties are to be developed in order to meet specific requirements. For example, high-Q resonators are preferable for applications in nanorefractometry to improve the figure of merit,[26] whereas low-Q plasmonic dipole antennas can be used for surface-enhanced sensing and spectroscopy techniques, including surface-enhanced Raman scattering (SERS). In the latter case, dipolelike antennas are typically used to concentrate the energy of free propagating waves into small regions (i.e., hotspots) with high localization and electric field enhancement (FE).[8,9]

Examples of dipolelike resonators are the dipole antenna [Fig. 1(a)] and bowtie antenna [Fig. 1(b)] placed on a dielectric substrate, with the gap between the two antenna arms functioning as a controllable hotspot. The triangular pointed particles in the bowtie configuration are constructed so as to take the advantage of not only the FE from the plasmonic resonance but also the electrostatic lightning rod effect from sharp corners. It is important to note that both resonance frequency and FE in the gap between the antenna arms of a dipole or bowtie antenna are highly sensitive to the geometrical and material parameters, such as bow (taper) angle, gap width, length of the arms of the antenna, dielectric permittivities of the substrate, and cladding.[9] We believe that the triangular shape typically used for the bowtie arms may lead to the loss of constructive interference of the plasmons due to their different optical paths between the bowtie vertex and different points on the opposite sides of the triangular bowtie arms. This is likely to cause a complex interference pattern for the plasmon in the resonator arms with rather poor predictability (rapid variations) of the field distribution, frequency response, and FE with changing geometrical and material parameters of the structure.[9] It could be expected that circular sectorlike bowtie arms [Figs. 1(c) and 1(d)] may alleviate this problem because in this configuration the optical paths between the vertex and different points on the circular edge of a bowtie arm are equal, and this should improve predictability of the frequency response and FE in the resonator. However, a detailed analysis of such circular bowtie resonators is needed.

Nanosized antennas and resonators may, in general, be categorized as being constructed from either insulator-metal-insulator (IMI) or metal-insulator-metal (MIM) configurations. For example, the conventional dipole and bowties antennas in the form of metal nanostrips on a dielectric substrate fall within the category of IMI structures. For structures with a large length-to-thickness ratio, theoretical[10–16] and experimental[13,27,28] works have demonstrated that the plasmonic resonances in nanoantennas can be interpreted as standing waves of slow surface plasmons (SSPs) for IMI structures and gap surface plasmons (GSPs) for MIM configurations. For MIM resonators involving GSPs,[12,14,15,27,28] it was found that they typically exhibit substantially lower radiation losses compared to IMI antennas.[12] As a result, the Q-factors for the MIM plasmonic resonators involving retardation and GSPs were predicted to approach ~ 20, which is close to the quasistatic limit.[29] The proposed use of the antibonding plasmonic modes in dipole IMI antennas[30] to increase the

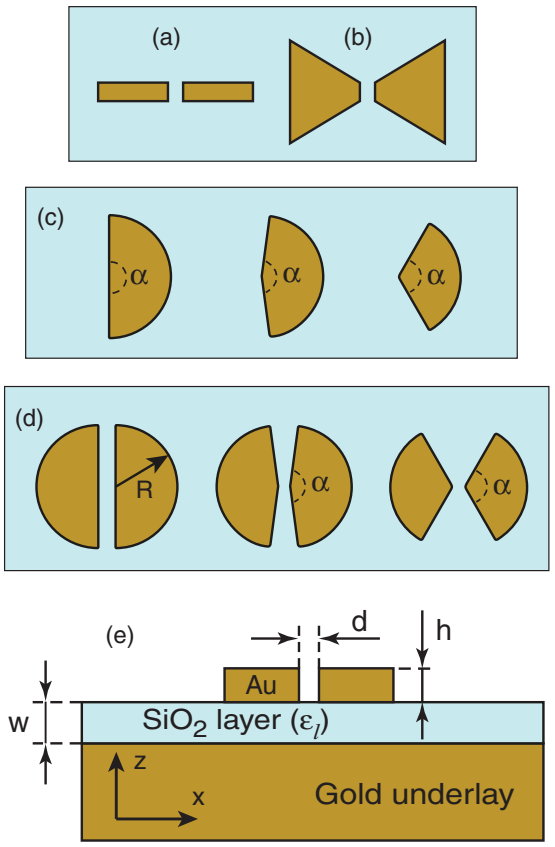

FIG. 1. (Color online) Plasmonic nanoantennas. (a) The dipole plasmonic antenna with two metal strips separated by a nanogap on a dielectric substrate. (b) The conventional bowtie plasmonic antenna with the triangular shape of the arms on a dielectric substrate. (c) Individual GSP resonators with circular (sectorlike) shape and different taper (bow) angles $\alpha = 180^\circ$, 165°, and 120° on a thin dielectric layer overlaying a thick gold underlay. (d) Bowtie GSP resonators with circular (sectorlike) shape of the resonator arms of radius R; tip-to-tip gap width is d. (e) The vertical cross section of a GSP bowtie resonator with the width d of the separating gap, thickness h of the gold nanoparticles forming the bowtie, and thickness w of the SiO_2 layer on a thick gold underlay; the axes of coordinates are as shown in the figure.

related Q-factors up to ~30 was achieved at the expense of losing local field enhancement in the gap between the antenna arms, reduction in the field localization, and low excitation efficiency, which are the significantly impeding factors for the practical use of such plasmonic resonances. Although MIM resonators are interesting for high-Q applications with strong local field enhancement and localization, the analysis of bowtie-type structures with GSPs has not, to the best of our knowledge, been conducted so far. Though two recent papers attempted the numerical and experimental investigation of plasmonic resonators in the form of metal nanodisks on a continuous thin dielectric film on a metal underlay,[31,32] no analysis of bowtie structures or the contribution of GSPs to the observed resonances was presented. The obtained results were investigated and interpreted as a quasistatic resonance in the disk, red-shifted by the near-field interaction between the gold nanodisk and its electrostatic image in the metal substrate (thick gold underlay).[31,32]

In this paper, we present a detailed theoretical and numerical analysis of an alternative type of bowtie structures supporting resonances with GSPs [Figs. 1(c)–1(e)]. In contrast to the usual triangular bowtie configuration [Fig. 1(b)], we will consider circular sectorlike bowties [Figs. 1(c) and 1(d)]. Only large bow (taper) angles of the circular bowties, which are rather close to 180°, will be considered. Such large taper angles make a direct comparison with triangular bowties[9] difficult, but will reveal new important physical phenomena in such structures and demonstrate their expected good predictability with varying geometrical parameters of the structure. In particular, the GSP bowtie response characteristics (including FE and typical scattering and absorption cross sections) are investigated as functions of the geometrical parameters, such as width of the gap between the bowtie arms and thickness of the dielectric layer separating the bowtie structures from the thick gold underlay [Fig. 1(e)]. It is shown that two distinct modes (with close resonant wavelengths) can be efficiently excited in the GSP bowtie configurations. One of these modes, corresponding to a low-Q resonance, is characterized by the domination of the dipolelike charge distribution in the bowtie arms, and the other mode corresponding to a high-Q resonance displays the dominance of the quadrupolelike charge distribution. The quality factors for the high-Q quadrupole resonance are predicted to approach or even exceed the quasistatic limit.[29] Detailed physical interpretation of the obtained results is presented.

II. RESONATOR CONFIGURATIONS AND CALCULATION PROCEDURE

The individual GSP bowtie resonators [Fig. 1(c)] consist of a gold nanoparticle in the form of a half-disk or sector with the radius R, taper angle α, and thickness $h = 60$ nm placed onto a thin dielectric SiO_2 layer with the relative permittivity $\varepsilon_l = 1.77$ (the experimentally measured value) and thickness w, deposited onto a thick gold underlay whose thickness is much larger than the skin depth. The same parametrization is used for the GSP bowtie resonators [Figs. 1(d) and 1(e)], although with the additional parameter d describing the tip-to-tip gap width between the bowtie arms. Where some of the parameter values are not explicitly stated in the text below or in the figure captions, these values are assumed to take on the nominal values $R = 150$ nm, $\alpha = 165^\circ$, $w = 28$ nm, and $d = 50$ nm. The vertex of the sectorlike gold nanoparticles with the taper angle α is assumed to be rounded with the radius of curvature $r = 10$ nm, while all other sharp edges are rounded with the radius of 5 nm. Because there is no vertex in a sector with the taper angle $\alpha = 180^\circ$ [the first nanoparticle in Fig. 1(c)] no rounding with the radius $r = 10$ nm is applicable in this case. The values for the gold permittivity at different incident wavelengths are taken from Ref. 33. The domain above the resonant structure (cladding) is assumed to be air. The analysis is conducted using the finite-element approach in the commercially available software package COMSOL MULTIPHYSICS. The considered three-dimensional structures are illuminated from the top using a monochromatic plane wave with the electric field amplitude E_0, linearly polarized along the x axis. For all geometrical configurations, the simulation domain is truncated using perfectly matched layers

in order to suppress artificial scattering from the truncation boundaries.[34] By dividing the total electromagnetic field into the incident field, specularly reflected field from the SiO_2 layer on the gold underlay (but without the gold particles), and scattered field due to the presence of the gold particle, the scattering cross section σ_{sc} is calculated as[35]

$$\sigma_{sc} = \frac{1}{I_{in}} \int_{Hemisphere} \frac{1}{2} (\mathbf{E}_{sc} \times \mathbf{H}^*_{sc}) \cdot \hat{\mathbf{n}}\, dS, \quad (1)$$

where $I_{in} = \frac{1}{2\eta} E_0^2$ is the intensity of the incident wave, η the wave impedance, $\mathbf{E}_{sc}$ and $\mathbf{H}_{sc}$ are the scattered electric and magnetic fields, respectively, and the integration hemisphere surrounds the gold particle, with $\hat{\mathbf{n}}$ being the outward normal unit vector to the hemisphere. The absorption cross section σ_{abs} is defined as the time-averaged total dissipative losses inside the sectorlike gold nanoparticle(s), i.e.,

$$\sigma_{abs} = \frac{1}{I_{in}} \int_{Nanoparticle} \frac{1}{2} \omega \varepsilon''_{Au} |\mathbf{E}|^2 dV, \quad (2)$$

where ω is the angular frequency, ε''_{Au} is the imaginary part of the permittivity of gold, and $\mathbf{E}$ is the electric field inside the nanoparticle(s).

Field enhancement is defined as the electric field enhancement relative to the incident amplitude E_0 and calculated in vacuum at the rounded vertex of the sectorlike gold nanoparticle (or in the middle of the straight side of the half-disk at $\alpha = 180^o$) at the level of $h/2$ (i.e., 30 nm above the SiO_2 layer). The quality factors (Q factors) for the considered configurations are calculated as the ratio $Q = \lambda_{res}/\Delta\lambda$, where λ_{res} and $\Delta\lambda$ are the resonance wavelength and the full-width-at-half-maximum of the resonance in the squared FE curves, respectively.

III. INDIVIDUAL GAP PLASMON RESONATORS

We commence our analysis of GSP bowtie structures from the consideration of individual GSP resonators [Fig. 1(c)]. The calculated scattering and absorption cross sections and FE of the considered individual GSP resonators are presented in Fig. 2 as functions of incident wavelength and clearly display resonant behavior. There are two types of resonances manifested by the maximums on the curves at ~700 nm and between the wavelengths of ~800 nm and ~900 nm (Fig. 2). The three strong maximums between the ~800 nm and ~900 nm demonstrate that the respective resonant wavelengths experience blue shift with decreasing taper angle α. At the same time, the resonant wavelengths for the resonances at ~700 nm are practically independent of α at the considered large taper angles. Another significant difference is the relative resonance strength. The maximums between ~800 nm and 900 nm appear significantly higher than those at ~700 nm, which is an indication of more efficient coupling of the incident radiation into these resonances.

It is argued that plasmonic coupling across the separating thin dielectric (SiO_2) layer between the gold nanoparticle and the thick gold underlay [Fig. 1(e)] plays an important role for both resonances. For example, at small thicknesses w of the separating layer (where w is much smaller than the wavelength), there is a distinct nanogap between the

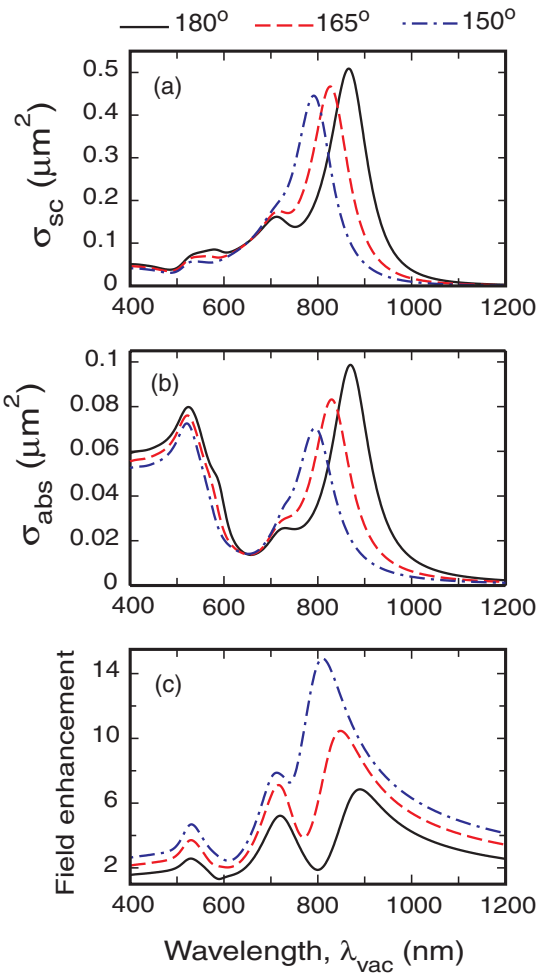

FIG. 2. (Color online) The calculated typical dependencies of (a) scattering cross section, (b) absorption cross section, and (c) FE on wavelength of the incident radiation. The structural parameters are the nominal values, and the taper angles α are as indicated.

nanoparticle and the gold underlay, and GSPs can exist in such a structure, experiencing multiple reflections from the terminations of the nanoparticle. As a result, Fabry-Perot-type resonances involving GSPs can occur in the structure. We believe that the predicted resonances between ~800 nm and ~900 nm and at ~700 nm in Fig. 2 are related to excitation and multiple reflections of such GSPs. The two different types of the predicted resonances and their behavior can then be explained by different types of the involved GSP modes and their distinct charge and field distributions (Fig. 3). For example, Fig. 3 shows similarities and significant differences between the typical field distributions in the modes corresponding to the resonances between ~800 nm and ~900 nm [Figs. 3(a) and 3(b)] and the resonances at ~700 nm [Figs. 3(c) and 3(d)]. Firstly, for both types of modes the field is mainly concentrated within the gap between the nanoparticle and the gold underlay [Figs. 3(b) and 3(d)]. This is a demonstration of the similar nature of these mode types in the sense that they are both formed by GSPs experiencing multiple reflections from the terminations of the nanoparticle.[14] On the other hand, the distributions of the z component of the

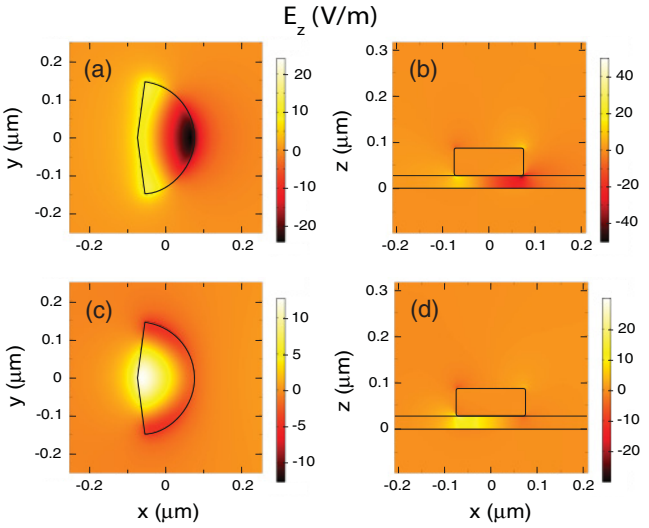

FIG. 3. (Color online) Distributions of the z component of the electric field in an individual sector-shaped GSP resonator with the taper angle $\alpha = 165^{o}$, the incident bulk wave is assumed to have the amplitude $E_0 = 1$ V/m, and the other parameters are as for Fig. 2. (a), (b) The E_z distributions for the resonance mode at $\lambda_{vac} = 848$ nm. (c), (d) The E_z distributions for the resonance mode at $\lambda_{vac} = 717$ nm. (a), (c) The typical E_z distributions in the x-y plane in the middle of the separating SiO_2 spacer. (b), (d) The typical E_z distributions in the x-z plane passing through the tip of the rounded vertex of the sector-shaped nanoparticle.

field in the x-y plane [Figs. 3(a) and 3(c)] are significantly different for the two resonance modes. The field distribution in the GSP mode shown in Fig. 3(a) (corresponding to the resonances between ∼800 nm and ∼900 nm in Fig. 2) is produced by the charge distribution in the nanoparticle with significant dipole moment along the x axis, whereas the mode in Fig. 3(c) (corresponding to the resonances at ∼700 nm in Fig. 2) is dominated by the quadrupolelike charge distribution in the nanoparticle along the y axis.

Importantly, increasing thickness w of the separating layer changes the resonance wavelength but not the typical patterns of the charge distribution in the nanoparticle. Even if $w \to \infty$ (a nanoparticle on an infinite dielectric substrate), the typical field distributions in the considered two resonance modes remain practically the same [Figs. 4(a) and 4(b)]. A noticeable difference is that both modes appear significantly blueshifted [compare Figs. 2 and 4(c)], which is the consequence of the transformation of the GSP in the gap (at small values of w) into the SSPs at large values of w. The transformation of GSPs into SSPs with increasing w is a natural consequence of the evolution from a MIM to an IMI configuration,[15] Therefore, at any finite thickness of the separating SiO_2 layer, both the resonance modes have the properties of SSPs and GSPs, with the SSP properties dominating at large values of w, and GSP properties dominating at small values of w. Hence, in the following we term the modes dipole GSP mode [Fig. 3(a)] and quadrupole GSP mode [Fig. 3(c)], respectively, highlighting the dominance of GSP properties for nanosized spacer thicknesses.

The comparative weakness of the resonances at ∼700 nm in Fig. 2 is related to the fact that the excitation of the

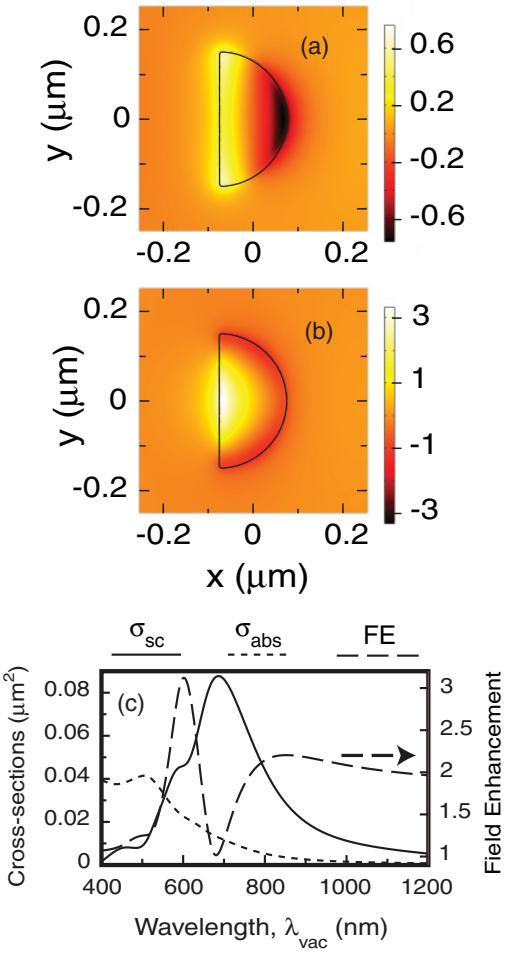

FIG. 4. (Color online) (a), (b) Distributions of the z component of the electric field in an individual semicircle ($\alpha = 180^{\circ}$) nanoparticle resonator on an infinite SiO_2 substrate ($w = +\infty$) at the distance 14 nm below the interface between the nanoparticle and the SiO_2 substrate (this distance was taken to match the considered plane with the field distribution used in Fig. 3). (a) The dipolelike mode at $\lambda_{vac} \sim 700$ nm, and (b) the quadrupolelike mode at $\lambda_{vac} \sim 600$ nm. (c) The dependencies of the scattering and absorption cross sections and FE in the considered nanoparticle resonator as functions of incident wavelength.

quadrupole GSP mode with the dominant quadrupolelike charge distribution along the y axis is inefficient by the incident bulk radiation with the polarization along the x axis. Therefore, we have only weak coupling between the generating bulk radiation and the quadrupole mode of the GSP resonator. On the contrary, the coupling efficiency for the dipole GSP mode is significantly higher, which leads to much higher resonances between ∼800 nm and ∼900 nm in Fig. 2. For the nanoparticle on the infinite SiO_2 substrate, the excitation of the modes is only apparent in the scattering cross section and not the absorption cross section [Fig. 4(c)]. This is a natural consequence of the weak field localization for $w \to \infty$ and the dominance of scattering loss for relatively large (i.e., compared to the quasistatic limit) particles. Also, the blueshift of the scattering cross section maximum for the dipole mode [at ∼700 nm on the solid curve in Fig. 4(c)] compared to the respective maximum of the FE [at ∼850 nm on the dashed

curve in Fig. 4(c)] is due to the depolarization effect in the nanoparticle.[36]

Reducing taper angle α but leaving it relatively close to 180° results in different rates of changing the typical size of the charge distributions in the dipole and quadrupole modes in the particle, which is equivalent of different rates of changing the efficient size of the resonator for the dipole and quadrupole modes. Indeed, the typical charge separation along the x axis in the dipole mode (i.e., the distance between the centers of the negative and positive charges in this mode) decreases linearly with the small angle $\delta = (180^\circ - \alpha)/2$ [compare Figs. 3(a) and 4(a)]. At the same time, the typical charge separation along the y axis in the quadrupole mode decreases quadratically with the small angle δ [compare Figs. 3(c) and 4(b)]. Consequently, the quadrupole resonance at ~700 nm in Fig. 2 with the dominant charge oscillations along the y axis [Figs. 3(c) and 4(b)] does not noticeably depend on taper angle α, whereas the dipole resonance with the dominant charge oscillations occurring along the x axis [Figs. 3(a) and 4(a)] moves to shorter wavelengths with decreasing α (Fig. 2).

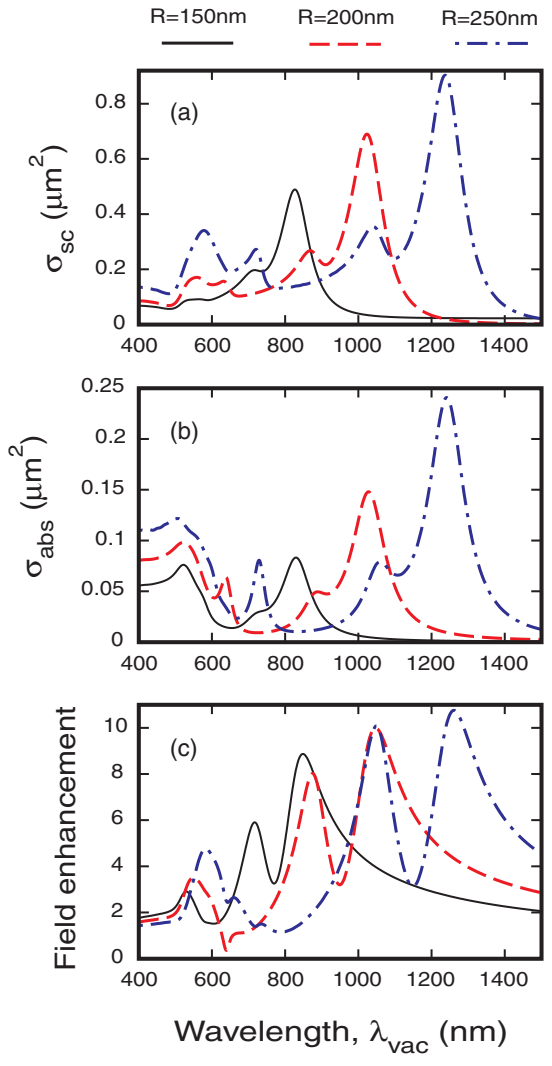

FIG. 5. (Color online) The dependencies of (a) scattering cross section, (b) absorption cross section, and (c) FE at the rounded vertex of the sectorlike gold nanoparticle on wavelength of the incident radiation for the three different radii $R = 150$ nm, 200 nm, and 250 nm.

In order to better understand the possibility of tuning the resonances, we investigated how the resonances are affected by changing the radius R of the sectorlike nanoparticle (Fig. 5). It is seen that the resonance wavelengths of both the quadrupole GSP resonance ($\lambda_{res} \approx 720$ nm, 875 nm, and 1050 nm) and dipole GSP resonance (≈850 nm, 1050 nm, and 1260 nm) increase in approximately the same proportions as the structural dimension ($R = 150$ nm, 200 nm, and 250 nm). This (approximately) linear relationship between the resonance wavelength and the structural dimension is in fact consistent with previous findings for GSP resonances.[14,37]

An increase in the structural dimension of the nanoparticle will automatically increase both the scattering and absorption losses [Figs. 5(a) and 5(b)]. However, the increase in FE of the quadrupole GSP mode compared to the dipole mode with increasing R [Fig. 5(c)] is an interesting observation if taking into account that the quadrupole GSP mode is not more efficiently excited for larger nanoparticles [see Figs. 5(a) and 5(b)]. This can be explained by the fact that increasing the nanoparticle dimension R results in increasing the resonant wavelength, which is associated with substantially weaker dissipation in the gold when moving away from the optical wavelengths into the near infrared. The increase in FE for larger resonance wavelengths is also in accordance with previous results on GSP resonators.[14]

IV. GAP PLASMON BOWTIES

The conducted numerical analysis and typical field distributions for the individual GSP resonators, presented in the previous section, suggest that we have found and described two significantly different types of modes in the considered GSP resonator structures. This result may have significant general implications for the consideration, optimization, and application of a range of plasmonic nanostructures and resonators based on the MIM configurations. However, only weak coupling of the quadrupole GSP modes to the incident bulk radiation, and the resultant rather weak resonances (Figs. 2 and 5) may be an obstacle on the way to successful application of these discovered resonances and their potential benefits including high-Q factors and potentially strong local field enhancements. Therefore, in this section, we demonstrate that using GSP bowtie structures enables full realization of the unique potentials of the new plasmonic resonant structures involving GSPs.

Figure 6 shows the typical scattering and absorption cross sections and FE for the GSP bowtie resonator structures. The major feature of the presented curves in Fig. 6 is the major increase of the strength of the resonance associated with the quadrupole GSP mode, which is manifested by the substantial increase of the respective maximums at ~700 nm, making the quadrupole resonance the dominant feature of the absorption and FE spectra [Figs. 6(b) and 6(c)]. We argue that this is likely to be caused by more efficient coupling between the incident radiation and the quadrupole GSP mode in the bowtie resonators, compared to the individual resonators. Such more efficient coupling occurs through the gap between the two

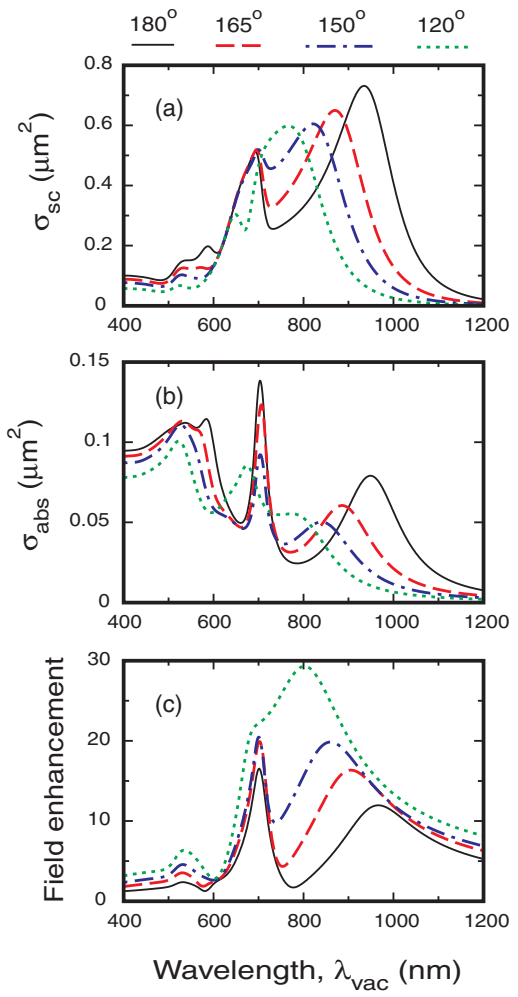

FIG. 6. (Color online) The calculated dependencies of (a) scattering cross section, (b) absorption cross section, and (c) FE for the GSP bowtie resonators on wavelength of the incident radiation. The taper angles α are as indicated for the presented curves.

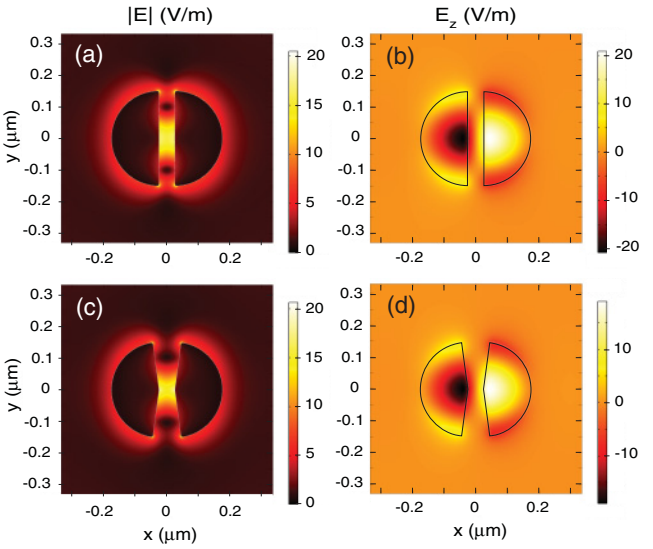

FIG. 7. (Color online) (a), (c) Distributions of the magnitude of the electric field $|E|$ at the height $h/2$ (i.e, 30 nm above the SiO_2 spacer) of the quadrupole modes of the bowtie GSP resonators with the two different taper angles: (a) $\alpha = 180^\circ$ and (c) $\alpha = 165^\circ$. (b), (d) Typical distributions of the z component of the electric field in the middle of the SiO_2 spacer for the quadrupole modes of the bowtie GSP resonators with the same two taper angles: (b) $\alpha = 180^\circ$ and (d) $\alpha = 165^\circ$.

bowtie arms owing to the more efficient scattering of light into the quadrupole mode. The result is a major increase of the respective levels of FE and the absorption cross section [Figs. 6(b) and 6(c)].

It is clear from Fig. 6 that a spectrum with two well-separated GSP modes is only possible for taper angles close to 180°. For angles $\alpha \leqslant 120^\circ$ the two modes begin to overlap, thereby significantly changing the physics of the resonance(s). Although the study of $\alpha \leqslant 120^\circ$ might show further interesting optical properties (e.g., high FE [Fig. 6(c)]), we dedicate this paper only to the situation of two spectrally well-separated modes with distinctly different optical properties. The advantage is the existence of both a high-Q and low-Q modes with close resonance wavelengths (and different taper angle dependencies) in a single structure that gives more design freedom and broadens the spectrum of possible applications.

Figure 7 illustrates the typical field distributions in the quadrupole GSP modes and demonstrates only weak dependence of these distributions on taper angle variations near 180°. This highlights stability and predictability of the spectral response in the proposed structures with respect to variations of the geometrical parameters (see also Fig. 6), which is contrary to what was predicted for the conventional triangular bowtie structures.[9] The field distributions in Fig. 7 also demonstrate the important relation between FE in the gap [Figs. 7(a) and 7(c)] and FE in the dielectric spacer [Figs. 7(b) and 7(d)]. Although, because of the metal-dielectric boundary conditions, the electric field is mainly x polarized in the gap and z polarized in the dielectric spacer, the typical values of FE are approximately the same in all subplots in Fig. 7. This highlights an important conclusion that FE in the considered resonances approximately equally occurs in the gap and in the dielectric spacer. In particular, this effect may lead to a significant practical benefit of the considered structures for the design of efficient photodetectors and photovoltaic devices that are typically heavily dependent upon strong local field enhancement and localization within thin dielectric layers.

The argument that the quadrupole GSP mode is mainly generated through the separating gap between the bowtie arms is further supported by the results presented in Fig. 8 for different values of the separation d. For example, Fig. 8(b) shows that the resonant absorption levels for the quadrupole mode are small at small separations, such as, for example, $d =$ 15 nm. Increasing separation d results in a significant increase of the resonant absorption level, which means increasing efficiency of coupling of the bulk radiation into the quadrupole GSP mode. By comparing Figs. 6 and 8, it is noticed that separations around $d \sim 50 - 75$ nm are optimal for the excitation of the quadrupole GSP mode. Further increase in d results in decreasing quadrupole resonance (Fig. 8), eventually leading to individual GSP resonators (Figs. 2 and 5) with only weak quadrupole GSP resonances. It can also be seen

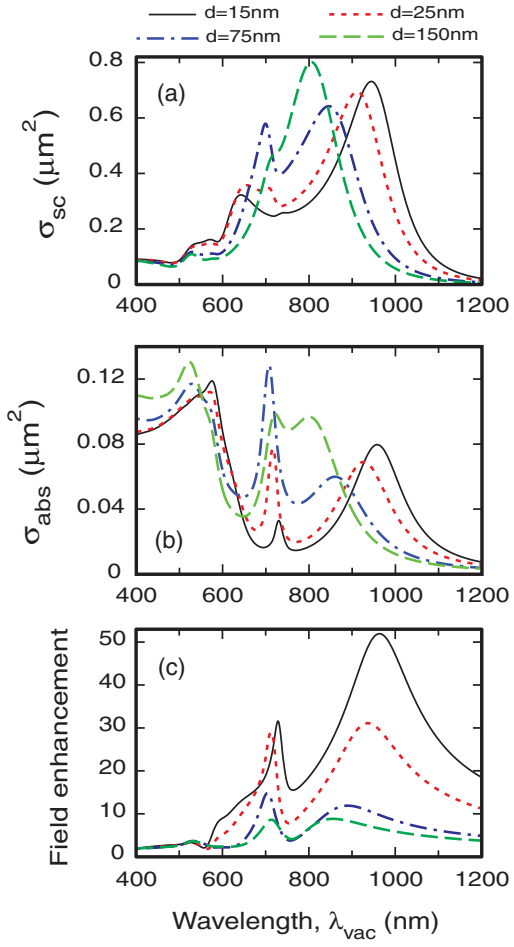

FIG. 8. (Color online) The dependencies of (a) scattering cross section, (b) absorption cross section, and (c) FE on wavelength of the incident radiation for different separations d between the bowtie arms.

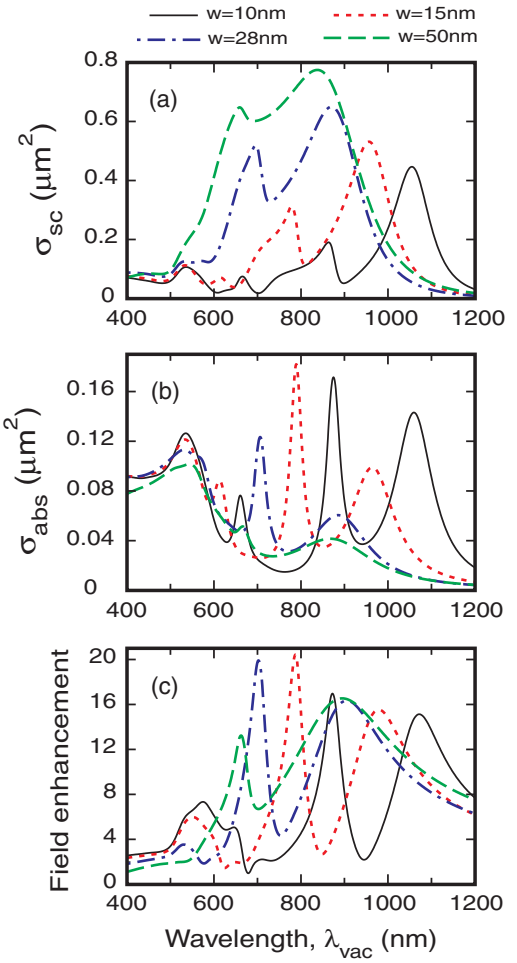

FIG. 9. (Color online) The dependencies of (a) scattering cross section, (b) absorption cross section, and (c) FE on wavelength of the incident radiation for different thicknesses of the SiO_2 spacer w.

that separation d between the bowtie arms does not influence significantly the resonant wavelength of the quadrupole GSP resonance, whereas the dipole resonance is blueshifted with increasing d (Fig. 8).

Although an optimal separation distance d can be found for the excitation of the quadrupole GSP mode, it does not typically correspond to the maximum FE [see Figs. 8(b) and 8(c)]. This is because FE always increases with decreasing separation distance if we assume the same efficiency of excitation of the quadrupole mode. As a result, we see the maximum FE in the quadrupole GSP mode for the smallest considered gap $d = 15$ nm [the solid curve in Fig. 8(c)]. However, the almost equal levels of FE in the quadrupole GSP mode for $d = 15$ nm and $d = 25$ nm [see the solid and dotted curves in Fig. 8(c)] result from the counteracting effect of decreasing efficiency of excitation of the quadrupole GSP mode in a very narrow gap between the bowtie arms. The situation is different for the dipole GSP mode as it is approximately equally efficiently excited for small gaps, hence the large level of FE > 50 for $d = 15$ nm.

The resonant wavelength for the quadrupole GSP resonance experiences blueshift with increasing thickness w of the SiO_2 spacer (Fig. 9). This is expected for both the quadrupole and dipole GSP modes, because increasing thickness w results in increasing wavelength of GSP due to weaker coupling across the gap, and this means that the resonant wavelength must decrease for fixed dimensions (radius R) of the resonator (Fig. 9). Another interesting conclusion that follows from Fig. 9 is that there exists an optimal thickness w at which the quadrupole GSP resonance is the strongest. This optimal thickness is $w_{opt} \sim 15$ nm for the considered structures [Figs. 9(b) and 9(c)]. If the values of w are very small ($w < 15$ nm), then the efficiency of coupling of the energy of the incident bulk radiation into GSPs is poor (tending to zero where $w \to 0$). On the other hand, if w is relatively large ($w > 15$ nm), then the leakage losses from the resonator significantly increase, also resulting in reduction of the resonance strength. It follows from here that there is $w = w_{opt}$ at which both the absorption cross section [Fig. 9(b)] and FE [Fig. 9(c)] achieve their maximum values for the quadrupole GSP resonance. The sharpness of the dipole GSP resonance increases with decreasing w (Fig. 9). This is in agreement with reducing radiation losses from a GSP mode with decreasing spacer thickness due to stronger confinement of the field in the dielectric spacer. A similar effect is not obvious for the quadrupole GSP mode (Fig. 9), which is

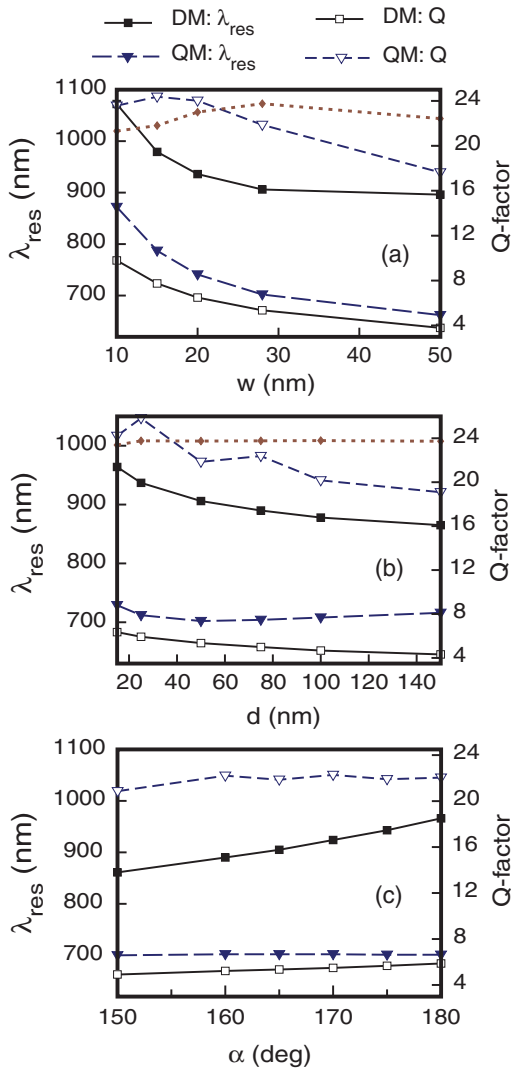

FIG. 10. (Color online) The dependencies of the resonant wavelengths λ_{res} and resonator Q factors on (a) thickness of the SiO_2 layer w, (b) separation between the bowtie arms d, and (c) taper angle α for the quadrupole and dipole GSP resonances in the considered GSP bowtie structures. The other structural parameters take on the nominal values. DM and QM stand for the dipole and quadrupole modes, respectively. The dotted curves with the solid dots represent the dependencies of the Q factor in the quasistatic limit.[29]

because radiation losses are already substantially suppressed for the dominant quadrupole charge distribution.

One of the important outcomes demonstrated by Figs. 4(c), 9, and 10(a) is that the GSP resonators and bowties may display significantly better resonance characteristics (Fig. 9), including significantly higher values of the Q factor [Figs. 9 and 10(a)], compared to the corresponding particle resonances (Fig. 4). This is the case for both the dipole and quadrupole GSP modes (see, for example, the increasing quality factors for both these resonances with decreasing spacer thickness [Fig. 10(a)]). Physically, this is related to the reduced leakage losses from the GSP modes at small spacer thickness, compared to particle plasmons.[12–15]

The Q factors and resonance wavelengths of both the quadrupole and dipole GSP modes are presented in Fig. 10 as a function of thickness of the SiO_2 spacer w, separation between the bowtie arms d, and taper angle α. The major outcome that can be seen from Fig. 10 is that the calculated Q factors for the quadrupole GSP resonances are indeed substantially higher than those for the dipole resonances (4–5 times larger). This is one of the major features of the considered GSP bowtie structures. Furthermore, the calculated Q factors for the quadrupole GSP resonances at small SiO_2 spacer thicknesses w and small separations d appear somewhat higher than the quasistatic limit[29] [Figs. 10(a) and 10(b)]. Finally, it is clear that in the case of large taper angles (resulting in spectrally separated quadrupole and dipole modes) the Q factor for both modes is only weakly dependent on taper angle [Fig. 10(c)]. It is actually only the resonance wavelength of the dipole mode that shows significant dependence on the taper angle [solid curve with filled squares in Fig. 10(c)].

V. CONCLUSIONS

In this paper, we have conducted the detailed theoretical and numerical investigation of a type of plasmonic resonators—bowtie antennas on the basis of MIM surface structures involving GSPs. The detailed analysis of the major properties of these structures was conducted to demonstrate a number of unusual and important features related to the formation and behavior of the resonance modes in the proposed structures. In particular, two physically and optically different GSP plasmonic modes with close resonant wavelengths were shown to exist in the considered plasmonic Fabry-Perot-like resonators. Both these modes are formed by GSPs generated in the dielectric spacer between the gold nanoparticle and the gold underlay, and experiencing multiple reflections from the terminations of the nanoparticle (these terminations thus working as mirrors in a Fabry-Perot resonator). The major physical difference between these two GSP modes is in the symmetry of the associated charge distributions in the nanoparticle with dominance of the dipolelike distribution (for the low-Q mode) and quadrupolelike distribution (for the high-Q mode). As a consequence of the charge distributions, the dipole GSP mode is efficiently excited in both individual resonators and bowtie configurations whereas the excitation efficiency of the quadrupole GSP mode is markedly improved in bowtie configurations due to the gap between the bowtie arms functioning as a way for light to efficiently couple into the quadrupole mode.

Detailed analysis and limit transitions for the major mode characteristics were conducted for different taper angles α, thicknesses of the dielectric spacer w separating the bowtie structure from the metal underlay, and separation between the bowtie arms d. It was found that only larger taper angles ($\alpha > 150^\circ$) should be used for the resonances to be spectrally well separated. Additionally, it was demonstrated that there exist optimal spacer thickness and gap width ensuring the best excitation condition for the quadrupole GSP mode in the considered bowtie structures. These parameters also control FE, with the gap width d being the dominant factor. Both the modes show strong FE up to $\sim 20-50$.

One of the major outcomes of this paper is the demonstration that the Q factors for the quadrupole GSP resonances in the proposed bowtie structures are consistently and substantially higher (by a factor of 4–5) than those for the dipole GSP resonances, despite the fact that both modes are efficiently excited. Furthermore, the predicted Q factors for the quadrupole GSP bowtie resonances at small values of w may exceed the previously determined quasistatic limit.[29]

The presented analysis and physical interpretations will be important for further analysis and investigation of MIM-based structures with potentially superior properties and characteristics (e.g., structures with two distinct high- and low-Q modes at close resonant wavelengths). The localization of the significant portion of the enhanced local field inside the thin dielectric layer opens opportunities for using the considered GSP resonators and their arrays to increase efficiency of photovoltaic devices and design photodetectors with enhanced signal-to-noise ratio. Easy and cost-effective fabrication of the considered structures (which requires only one lithography step) can form an efficient basis for other plasmonic applications such as nano-optical sensors (e.g., refractive index sensing) and SERS techniques, including single-molecule detection and identification.

ACKNOWLEDGMENTS

We acknowledge support for this work from the VELUX Foundation and from the Danish Council for Independent Research (the FTP project ANAP, Contract No. 09-072949).

*pors@mci.sdu.dk

[1] P. Bharadwaj, B. Deutsch, and L. Novotny, Adv. Opt. Photon. **1**, 438 (2009).
[2] L. Novotny and N. van Hulst, Nature Photon. **5**, 83 (2011).
[3] D. K. Gramotnev and S. I. Bozhevolnyi, Nature Photon. **4**, 83 (2010).
[4] J. Wessel, J. Opt. Soc. Am. B **2**, 1538 (1985).
[5] U. C. Fischer and D. W. Pohl, Phys. Rev. Lett. **62**, 458 (1989).
[6] K. B. Crozier, A. Sundaramurthy, G. S. Kino, and C. F. Quate, J. Appl. Phys. **94**, 4632 (2003).
[7] A. Sundaramurthy, K. B. Crozier, G. S. Kino, D. P. Fromm, P. J. Schuck, and W. E. Moerner, Phys. Rev. B **72**, 165409 (2005).
[8] P. Muhlschlegel, H.-J. Eisler, O. J. F. Martin, B. Hecht, and D. W. Pohl, Science **308**, 1607 (2005).
[9] H. Fischer and O. J. F. Martin, Opt. Express **16**, 9144 (2008).
[10] T. Søndergaard and S. I. Bozhevolnyi, Phys. Rev. B **75**, 073402 (2007).
[11] L. Novotny, Phys. Rev. Lett. **98**, 266802 (2007).
[12] S. I. Bozhevolnyi and T. Søndergaard, Opt. Express **15**, 10869 (2007).
[13] T. Søndergaard, J. Beermann, A. Boltasseva, and S. I. Bozhevolnyi, Phys. Rev. B **77**, 115420 (2008).
[14] T. Søndergaard, J. Jung, S. I. Bozhevolnyi, and G. Della Valle, New J. Phys. **10**, 105008 (2008).
[15] J. Jung, T. Søndergaard, and S. I. Bozhevolnyi, Phys. Rev. B **79**, 035401 (2009).
[16] A. Pors, M. Willatzen, O. Albrektsen, and S. I. Bozhevolnyi, J. Opt. Soc. Am. B **27**, 1680 (2010).
[17] P. Ghenuche, S. Cherukulappurath, T. H. Taminiau, N. F. van Hulst, and R. Quidant, Phys. Rev. Lett. **101**, 116805 (2008).
[18] A. Weber-Bargioni, A. Schwartzberg, M. Schmidt, B. Harteneck, D. F. Ogletree, P. J. Schuck, and S. Cabrini, Nanotechnology **21**, 065306 (2010).
[19] J. N. Farahani, D. W. Pohl, H.-J. Eisler, and B. Hecht, Phys. Rev. Lett. **95**, 017402 (2005).
[20] W. Zhang, L. Huang, C. Santschi, and O. J. F. Martin, Nano Lett. **10**, 1006 (2010).
[21] M. L. Juan, M. Righini, and R. Quidant, Nature Photon. **5**, 349 (2011).
[22] H. A. Atwater and A. Polman, Nature Mater. **9**, 205 (2010).
[23] L. Tang, S. E. Kocabas, S. Latif, A. K. Okyay, D.-S. Ly-Gagnon, K. C. Saraswat, and D. A. B. Miller, Nature Photon. **2**, 226 (2008).
[24] J. A. Schuller, E. S. Barnard, W. Cai, Y. C. Jun, J. S. White, and M. L. Brongersma, Nat. Mater. **9**, 193 (2010).
[25] A. Kinkhabwala, Z. Yu, S. Fan, Y. Avlasevich, K. Mullen, and W. E. Moerner, Nature Photon. **3**, 654 (2009).
[26] N. Verellen, P. V. Dorpe, C. Huang, K. Lodewijks, G. A. E. Vandenbosch, L. Lagae, and V. V. Moshchalkov, Nano Lett. **11**, 391 (2011).
[27] H. T. Miyazaki and Y. Kurokawa, Phys. Rev. Lett. **96**, 097401 (2006).
[28] P. Bouchon, F. Pardo, B. Portier, L. Ferlazzo, P. Ghenuche, G. Dagher, C. Dupuis, N. Bardou, R. Haidar, and J.-L. Pelouard, Appl. Phys. Lett. **98**, 191109 (2011).
[29] F. Wang and Y. R. Shen, Phys. Rev. Lett. **97**, 206806 (2006).
[30] J.-S. Huang, J. Kern, P. Geisler, P. Weinmann, M. Kamp, A. Forchel, P. Biagioni, and B. Hecht, Nano Lett. **10**, 2106 (2010).
[31] Y. Chu and K. B. Crozier, Opt. Lett. **34**, 244 (2009).
[32] Y. Chu, M. G. Banaee, and K. B. Crozier, ACS Nano. **4**, 2804 (2010).
[33] P. B. Johnson and R. W. Christy, Phys. Rev. B **6**, 4370 (1972).
[34] J. Jin, *The Finite Element Method in Electromagnetics* (Wiley, New York, 1993).
[35] J. Jung and T. Søndergaard, Phys. Rev. B **77**, 245310 (2008).
[36] K. L. Kelly, E. Coronado, L. L. Zhao, and G. C. Schatz, J. Phys. Chem. B **107**, 668 (2003).
[37] G. Della Valle, T. Søndergaard, and S. I. Bozhevolnyi, Opt. Express **16**, 6867 (2008).